



Longitudinal Data and a Semantic Similarity Reward for Chest X-ray Report Generation

14 Feb 2024 Aaron Nicolson^{a,*}, Jason Dowling^{a,b}, Doug Anderson^{c,d,e}, Bevan Koopman^{a,b}

^aThe Australian e-Health Research Centre, CSIRO Health and Biosecurity, Brisbane, Australia

^bSchool of Electrical Engineering & Computer Science, University of Queensland, Brisbane, Australia

^cImaging Associates, Melbourne, Australia

^dSt Vincent's Hospital, Melbourne, Australia

^eMonash Health, Melbourne, Australia

ARTICLE INFO

Article history:

2000 MSC: 92C55, 68T45, 68T50

Keywords: Chest X-ray report generation, Radiology report generation, Image captioning, Natural language generation

ABSTRACT

The burnout rate of radiologists is high in part due to the large and ever growing number of Chest X-rays (CXRs) needing interpretation and reporting. Promisingly, automatic CXR report generation has the potential to aid radiologists with this laborious task and improve patient care. The diagnostic inaccuracy of current CXR report generators prevents their consideration for clinical trials. To improve diagnostic accuracy, we propose a CXR report generator that integrates aspects of the radiologist workflow and is trained with our proposed reward for reinforcement learning. It imitates the radiologist workflow by conditioning on the longitudinal history available from a patient's previous CXR study, conditioning on multiple CXRs from a patient's study, and differentiating between report sections with section embeddings and separator tokens. Our reward for reinforcement learning leverages CXR-BERT — which captures the clinical semantic similarity between reports. Training with this reward forces our model to learn the clinical semantics of radiology reporting. We also highlight issues with the evaluation of a large portion of CXR report generation models in the literature introduced by excessive formatting. We conduct experiments on the publicly available MIMIC-CXR and IU X-ray datasets with metrics shown to be more closely correlated with radiologists' assessment of reporting. The results demonstrate that our model generates radiology reports that are quantitatively more aligned with those of radiologists than state-of-the-art models, such as those utilising large language models, reinforcement learning, and multi-task learning. Through this, our model brings CXR report generation one step closer to clinical trial consideration. Our Hugging Face checkpoint (<https://huggingface.co/aehrc/cxrmate>) and code (<https://github.com/aehrc/cxrmate>) are publicly available.

© 2024 Elsevier B. V. All rights reserved.

1. Introduction

Burnout — a risk factor for significant mental illness — is increasingly prevalent amongst radiologists due to factors including high workloads and clinical documentation (Bailey et al.,

2022). Particularly in emergency departments, it is predicted that improving radiologists' efficiency through the automation of image interpretation and radiology reporting can reduce the burden placed on them and improve patient outcomes (Shen, 2021). With the Chest X-ray (CXR) being the most ubiquitous first-line imaging tool for chest assessment globally, automatic CXR report generation becomes a logical solution (Jones et al., 2021). While current CXR report generators utilising encoder-

*Corresponding author: email: aaron.nicolson@csiro.au;

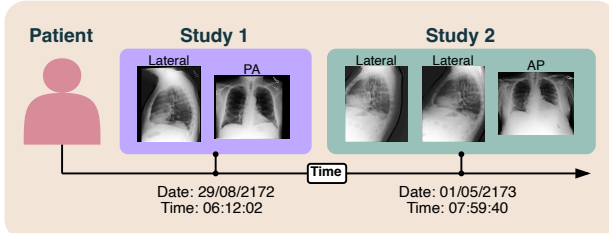


Fig. 1. A patient can have multiple CXR studies over time. Each study can consist of multiple images, often representing different views of the chest. Note that the year of each study has been modified for anonymisation purposes.

to-decoder models are promising, a significant improvement in diagnostic accuracy is required before clinical trial consideration.

Several factors about how CXRs are interpreted in a clinical setting have been overlooked in prior CXR report generation methods. We outline these factors — and how we leverage them to improve CXR report generation — in Figures 1 and 2. Figure 1 shows that a CXR study for a patient can consist of multiple images. A CXR image can be a frontal view of the patient — such as an *anteroposterior* (AP) or *posteroanterior* (PA) view — or a lateral view. Radiologists will interpret all images of a study in unison before writing a report, as each view contains important information (Gaber *et al.*, 2005). However, this is overlooked with most previous CXR report generation methods, where a separate report is generated per image, as shown in Figure 2 A (Chen *et al.*, 2020). This does not replicate real world radiologist reporting practice. Few models are conditioned on all images of a study if available, as shown in Figure 2 B (Miura *et al.*, 2021). Moreover, there has been no empirical evaluation comparing multi-image CXR report generation to single-image CXR report generation. Hence, we provide this evaluation as a contribution of our investigation.

Returning to Figure 1, we note that a patient can also have multiple studies over time (e.g., Study 1 and Study 2). A radiologist makes use of this longitudinal data by comparing the current study to previous studies and identifying key differences — which can aid diagnostic accuracy (Kelly, 2012). Although standard in the clinical setting, conditioning on longitudinal data has not been thoroughly investigated for CXR report generation (Wu *et al.*, 2022).

Motivated by this, we propose longitudinal, multi-image CXR report generation to improve diagnostic accuracy. Here, the model is not only conditioned on all images of a patient's current study, but also the report from their previous study if available, as shown in Figure 2 C. We accomplish this in a parameter efficient manner; we use Low-Rank Adaptation (LoRA) (Hu *et al.*, 2022) to adapt a multi-image CXR report generator to the task of longitudinal, multi-image CXR report generation where it is conditioned on the report of the previous study via a prompt. Evidence to support longitudinal, multi-image CXR report generation is given in Figure 3. The top plot shows the number of images per study, of which 55% have multiple images, while the bottom plot shows the number of studies per patient, of which 50% have more than one study. This

demonstrates that multiple images and longitudinal data can be frequently leveraged for CXR report generation.

In addition to this, we investigate a new domain-specific reward for reinforcement learning. Self-Critical Sequence Training (SCST) is a reinforcement learning algorithm for image captioning that mitigates the *exposure bias* problem (Rennie *et al.*, 2017).¹ When paired with a reward that captures the semantic similarity between the generated and radiologist reports, SCST is able to significantly improve the performance of a CXR report generator (Liu *et al.*, 2019). The choice of reward can have a large impact on performance, as demonstrated by the state-of-the-art reward based on RadGraph (Delbrouck *et al.*, 2022). This reward makes use of named entity recognition; it compares the entities and relations between the generated and radiologist reports.

Recently, CXR-BERT was proposed, a Transformer encoder pre-trained with contrastive representation learning that can place reports that are semantically similar close together in latent space, while placing those that are dissimilar farther apart (Boecking *et al.*, 2022). We propose a reward based on CXR-BERT, to force our model to learn the clinical semantics of radiology reporting. Specifically, the reward is formed via the cosine similarity between the generated and radiologist reports in CXR-BERT's latent space. We hypothesise that this better captures the semantic similarity between the generated and radiologist reports than the entities and relations of RadGraph.

By understanding and then translating the nuances of the radiologist workflow into a succinct neural architecture, as well as introducing a reward that captures the semantics of radiology reporting, our proposed model is able to generate radiology reports that are more closely aligned with those of radiologists than current CXR report generators, such as those leveraging large language models, reinforcement learning, and multi-task learning. We evaluate our model on the publicly available MIMIC-CXR and IU X-ray datasets (Johnson *et al.*, 2019; Demner-Fushman *et al.*, 2016) with metrics shown to be more closely correlated with radiologists' assessment of reporting (Yu *et al.*, 2023). Furthermore, the characteristics that lend CXR-BERT to being a suitable reward for reinforcement learning also make it appropriate as a metric for CXR report generation, hence, we introduce it here additionally as a metric. Finally, there is a lack of available code and model checkpoints in the literature, making it difficult for the field to progress. To overcome this, we provide our code repository and model checkpoints in an easily accessible manner. To summarise, the main contributions of this investigation are as follows:

1. A state-of-the-art CXR report generation model.
2. Integration of the radiologist workflow into CXR report generation; conditioning on all images of a patient's current study and the report from their previous study; the differentiation of report sections via section embeddings and separator tokens (described in Subsection 3.4).

¹Exposure bias refers to error accumulation during generation caused by the lack of exposure of a model to its own generated tokens during training (Rennie *et al.*, 2017).

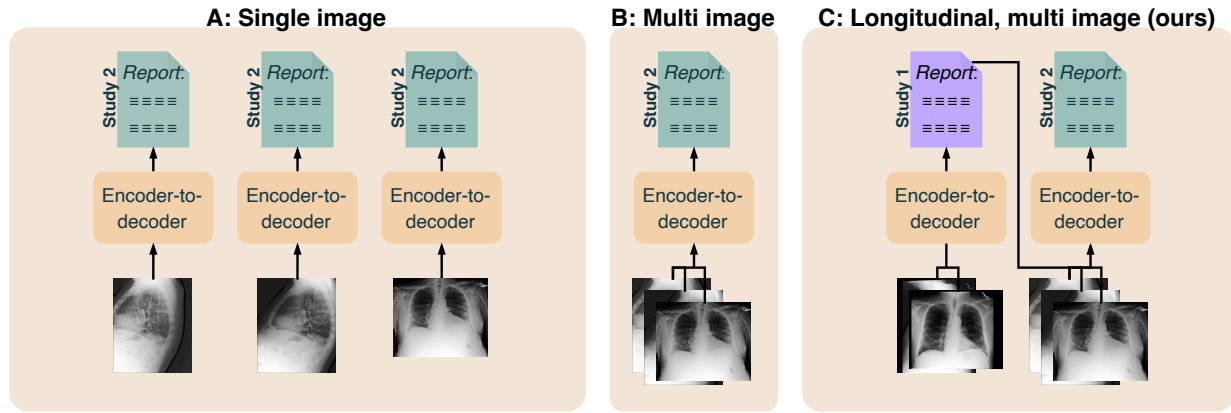


Fig. 2. CXR report generation conditioned on **A:** a single image of a study, **B:** all images of a study, and **C:** all images of a study, as well as the report of the previous study.

3. A reinforcement learning reward and metric based on CXR-BERT.
4. An experimental evaluation on the MIMIC-CXR and IU X-ray datasets (Johnson *et al.*, 2019; Demner-Fushman *et al.*, 2016) with metrics shown to be more closely correlated with radiologists' assessment of reporting (Yu *et al.*, 2023).
5. A comparison between the single-image, multi-image, and longitudinal, multi-image cases; a comparison between the CXR-BERT reward and other rewards in the literature; and a comparison with state-of-the-art CXR report generators in the literature.
6. Our Hugging Face checkpoint (<https://huggingface.co/aehrc/cxrmate>) and code (<https://github.com/aehrc/cxrmate>) are publicly available.
7. We also highlight issues pertaining to the evaluation of a large portion of CXR report generation models in the literature, in particular, where the fidelity of the labels to the original radiologist reports has been compromised due to excessive formatting. This is described in Subsection 3.4.
8. We develop a means of performing SCST with the generated report from the previous study, which is described in Subsection 3.2. Prompting with the *generated* report from the previous study, rather than the *radiologist* report from the previous study is important, as a radiologist report may not always be available in practice.

2. Related Work

The MIMIC-CXR dataset is publicly available and consists of radiographic studies performed at the Beth Israel Deaconess Medical Center in Boston, MA, between 2011–2016 (Johnson *et al.*, 2019). Each study includes a semi-structured free-text radiology report that describes the radiological findings of the images, written by a practising radiologist contemporaneously during routine clinical care. All images and reports were de-identified to protect privacy. MIMIC-CXR is the standard dataset used for CXR report generation evaluation, due to its relatively large size and high quality (Yu *et al.*, 2023). It is also one of the few CXR datasets that retains the metadata and

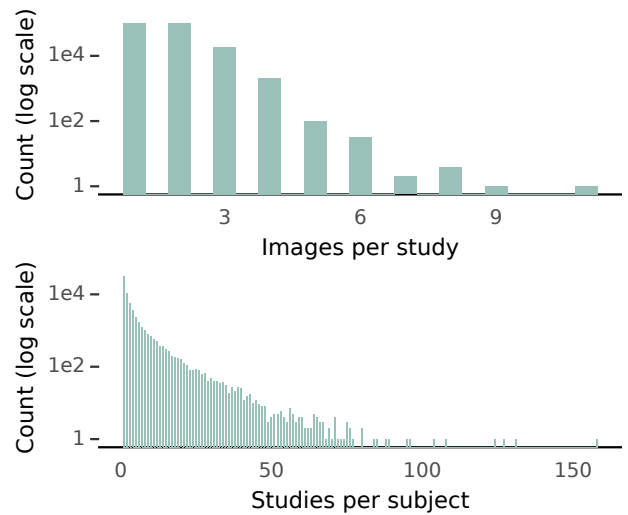


Fig. 3. Histograms of the training split of MIMIC-CXR (Johnson *et al.*, 2019). Top: multiple images are often taken for a single CXR study, thus motivating multi-image CXR report generation. Bottom: a patient often has multiple CXR studies over time, thus motivating our longitudinal, multi-image CXR report generation approach.

radiology reports of each patient's study, and is currently the sole publicly-available dataset to retain the longitudinal information between studies (Johnson *et al.*, 2019). We use it for model training and evaluation; it is further described in Subsection 3.5.1.

The IU X-ray dataset is also publicly available (Demner-Fushman *et al.*, 2016). It consists of radiology reports from two large hospital systems within the Indiana Network for Patient Care, along with associated images from the hospitals' picture archiving systems. The images and reports were de-identified automatically with subsequent manual verification. Only one study per patient was included in the dataset, where outpatient studies were targeted. Even though it is relatively small, IU X-ray is often used in pair with MIMIC-CXR for CXR report generation evaluation. Though longitudinal data cannot be leveraged with IU X-ray, we use it as a test set to assess. It is further described in Subsection 3.5.1.

CXR report generation is typically performed with an encoder-to-decoder model, with many recent studies proposing architectural improvements. Chen *et al.* (2020) proposed a “memory-driven” Transformer decoder (R2Gen), which was later developed into a “Cross-modal Memory Network” (CMN) (Chen *et al.*, 2021). Nicolson *et al.* (2023) compared different encoder and decoder architectures and pre-trained checkpoints, where it was found that the Convolutional vision Transformer (CvT) and DistilGPT2 performed best (CvT2DistilGPT2). Following CvT2DistilGPT2, we use CvT as the encoder for our model. However, we use a randomly initialised Transformer decoder with a tokeniser formed from the reports of MIMIC-CXR to establish a domain-specific vocabulary.

Others have proposed new objectives to improve the models understanding of the relationship between CXR and report. Yan *et al.* (2021) proposed a Weakly-supervised Contrastive Loss (WCL) between features of the CXR and radiologist report, where negative samples that were semantically closer to the radiologist report were given more weight. Najdenkoska *et al.* (2022) forced features of the CXR and radiologist report to be aligned in a latent space by formulating the report generation task as a conditional variational inference problem. For our model, we use the standard objectives for text-to-image generation associated with teacher forcing (Williams and Zipser, 1989) and SCST (Rennie *et al.*, 2017).

There are multiple investigations that demonstrate that conditioning CXR report generation on a patient’s previous study improves performance (Wu *et al.*, 2022; Dalla Serra *et al.*, 2023; Zhu *et al.*, 2023). For our investigation, we build upon these and address several of their weaknesses. For example, Wu *et al.* (2022) only included patients with four or more studies, while Zhu *et al.* (2023) only include patients with three or more studies from the MIMIC-CXR test set. Contrary to this, we do not exclude patients from MIMIC-CXR based on their number of studies — even those with only a single study are considered. This is a more difficult task for a longitudinal model, as longitudinal data is not favoured and the model must also handle cases that do not have a previous study. Furthermore, Wu *et al.* (2022); Dalla Serra *et al.* (2023); Zhu *et al.* (2023) considered only a single image from a patient’s study (in Wu *et al.* (2022); Dalla Serra *et al.* (2023) lateral views were excluded); our model considers all CXRs for a study, regardless of view. By performing longitudinal, multi-image CXR report generation rather than longitudinal, single-image CXR report generation, our model is more aligned with the radiologist workflow. Moreover, Wu *et al.* (2022); Dalla Serra *et al.* (2023); Zhu *et al.* (2023) made use of additional encoders to handle the previous study; for our model, we adopt a more parameter efficient solution by adapting a multi-image CXR report generator with LoRA to condition on the report of the previous study via a prompt. Furthermore, Wu *et al.* (2022); Dalla Serra *et al.* (2023); Zhu *et al.* (2023) conditioned only on the *radiologist* report from the previous study; in our investigation, we additionally consider the case of conditioning on the *generated* report from the previous study — as a radiologist report may not always be available in practice. Furthermore, Wu *et al.* (2022); Dalla Serra *et al.* (2023); Zhu *et al.* (2023) do not consider lon-

itudinal data with SCST. In this direction, we develop a means of performing SCST with the generated report from the previous study, as described in Subsection 3.2. Finally, the experiments from Wu *et al.* (2022); Dalla Serra *et al.* (2023); Zhu *et al.* (2023) are not reproducible; either there is no code, or there is no model checkpoint available, making them difficult to compare to.

Rewards for SCST that capture the semantic similarity between the generated and radiologist reports have significantly improved CXR report generation. Recently, Miura *et al.* (2021) proposed fact_{ENT} and $\text{fact}_{\text{ENTNLI}}$, two rewards that take advantage of Named-Entity Recognition (NER). Here, the number of entity matches between the generated and radiologist reports forms the basis of these rewards. Delbrouck *et al.* (2022) proposed a reward that was able to outperform fact_{ENT} and $\text{fact}_{\text{ENTNLI}}$ by leveraging RadGraph. RadGraph is a dataset of entities and relations from 500 MIMIC-CXR radiology reports that was used to train a model to jointly predict the entities and relations from reports (Jain *et al.*, 2021). The reward compares the entities and relations between the generated and radiologist reports extracted using this model (RadGraph ER). In this investigation, we compare these rewards, amongst others, to the proposed CXR-BERT reward.

Recently, the MIMIC-CXR dataset has been used for multi-task learning, specifically of generative tasks, with the hypothesis that learning one task will improve learning the other tasks. Lee *et al.* (2023) proposed UniXGen, which leverages a Vector Quantisation Generative Adversarial Network (VQ-GAN) to discretise CXRs into discrete visual tokens. From this, UniXGen simultaneously learns to generate a report and other views of the patient. It was found that multi-task learning was beneficial to each task. LLM-CXR builds upon UniXGen by instruction-tuning a Large Language Model (LLM) conditioned on CXR features to perform either CXR report generation (CXR-to-report generation) or report-to-CXR generation (Lee *et al.*, 2024). LLaMA 2 (Touvron *et al.*, 2023) was used to generate instructions from the reports of MIMIC-CXR for instruction tuning. Through this, LLM-CXR was able to outperform UniXGen on both CXR-to-report generation and Visual Question Answering (VQA) tasks. Yang *et al.* (2023) proposed MedXChat, which jointly learned CXR-to-report generation, report-to-CXR generation, and VQA. MedXChat takes advantage of Stable Diffusion for report-to-CXR generation, and was shown to outperform LLM-CXR and UniXGen. One issue that pertains to these models is the discrepancies between how they split and format the MIMIC-CXR test set. This makes a comparison difficult. This is elaborated upon in Subsections 3.4 and 4.4. Nevertheless, we compare to these models, as they represent strong benchmarks.

As of late, a lot of attention has been paid to VQA for biomedical imaging — a more general task than CXR-based VQA. Med-Flamingo is a few-shot learner trained on image and text data from medical textbooks and PubMedCentral’s OpenAccess subset (Moor *et al.*, 2023). Given a few examples, it is able to adapt to a specific medical image-text task. LLaVA-Med is also trained on PubMedCentral’s OpenAccess subset (Li *et al.*, 2023). GPT-4 was used to generate instructions from

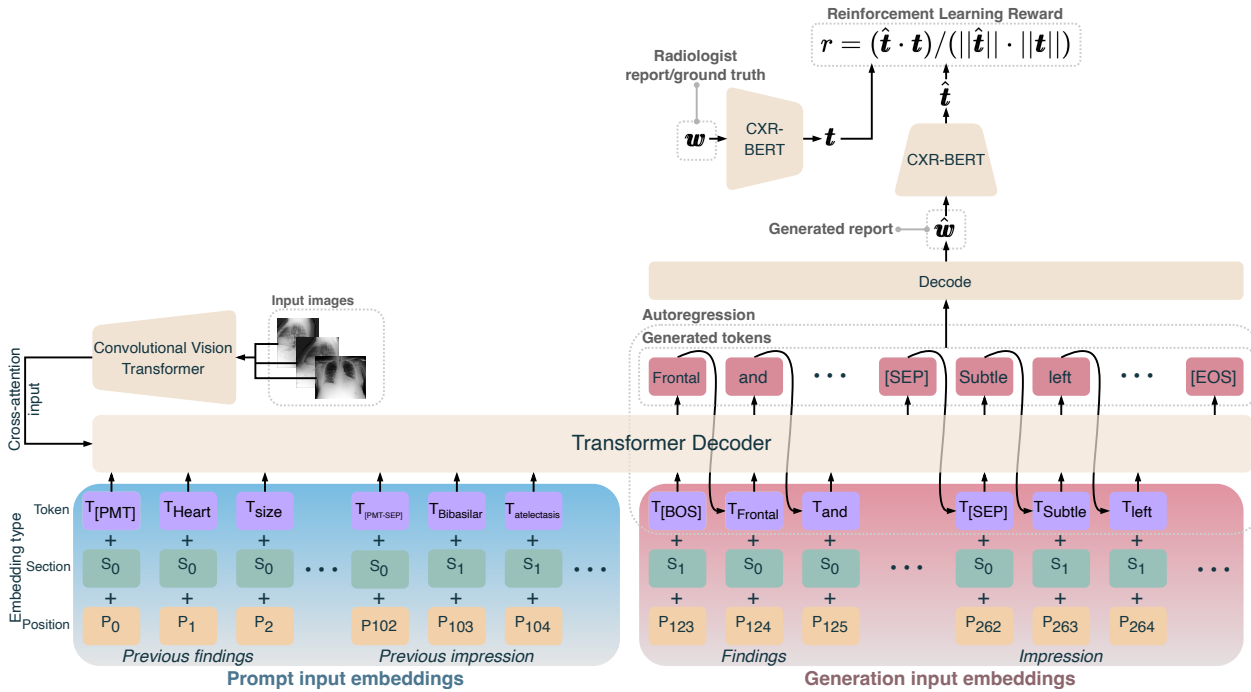


Fig. 4. Our proposed model: a longitudinal, multi-image CXR report generator trained with reinforcement learning using the CXR-BERT cosine similarity reward. The findings and impression sections from the reports of the current and previous studies are differentiated by section embeddings and separator tokens. The prompt is the report of the previous study.

captions to train LLaVA-Med for VQA. It was able to outperform previous state-of-the-art methods on three biomedical VQA tasks. In this study, we investigate how they perform on CXR report generation with no, or few-shot learning.

3. Methods

3.1. Longitudinal, Multi-image CXR Report Generation

Longitudinal, multi-image CXR report generation is defined here as conditioning the generation of a study’s report on all images of a study, as well as data from previous studies. Here, we prompt the decoder with the report of the previous study, as shown in Figure 4. To accommodate the prompt and the differentiation of the different sections, we adopt a schema influenced by pre-trained Transformer encoders (Devlin et al., 2019). The [PMT], [BOS], and [EOS] special tokens, indicate the beginning of the prompt, the beginning of the generated report, and the end of the generated report, respectively. The [PMT-SEP] and [SEP] special tokens indicate the separation between the findings and impression sections for the prompt and generated report, respectively. Moreover, [SEP] allows the findings and impression sections to be extracted from the generated report. Finally, the [NPF] and [NPI] special tokens, which denote “no previous findings” and “no previous impression”, respectively, are placeholders if no previous study exists. In addition, we add section embeddings to the input of the decoder to differentiate between the findings and impression sections.

Next, we describe prompting the decoder with the *radiologist* and *generated* reports from the previous study. Let $w^t = (w_1^t, \dots, w_M^t)$ and $\hat{w}^t = (\hat{w}_1^t, \dots, \hat{w}_N^t)$ denote the tokens (of

length M and N) of the radiologist and generated reports for the current study t , respectively. Either the radiologist report from the previous study w^{t-1} or the generated report from the previous study \hat{w}^{t-1} can be the prompt. In practice, conditioning on \hat{w}^{t-1} may be necessary, as w^{t-1} may not always be available. During training, w^{t-1} can be used as the prompt for teacher forcing or SCST, as it is readily available. However, using \hat{w}^{t-1} as the prompt during training is difficult, as described in the next subsection.

3.2. SCST With the Generated Report From the Previous Study as the Prompt

If a model was trained with the w^{t-1} prompt, and the \hat{w}^{t-1} prompt is used at test time, there will be exposure bias as the model did not observe the \hat{w}^{t-1} prompt during training. Hence, we aim to train with the \hat{w}^{t-1} prompt to reduce exposure bias when the \hat{w}^{t-1} prompt is used at test time.

Generating the \hat{w}^{t-1} prompt for each training example would be inefficient, as it would need to be performed before forward propagation (for teacher forcing) or autoregression (for SCST). Conveniently, the baseline of a study — which is a report generated with greedy search decoding during SCST — can be used as the \hat{w}^{t-1} prompt for the subsequent study of a patient in a later mini-batch. However, care must be taken to minimise the number of mini-batch updates between when the baseline was generated and when it is used as the \hat{w}^{t-1} prompt. This is because there can be a large drift in the distribution of the model’s parameters if too many mini-batch updates have occurred. If the drift is too large, the \hat{w}^{t-1} prompt may not be representative of what the model in the current mini-batch would generate. To

minimise this, we order a patient’s studies in subsequent mini-batches (where there cannot be more than one study per patient in a mini-batch and the order of the patients for each epoch is shuffled instead of the studies). This way, the baseline from the preceding mini-batch can be used as the $\hat{\mathbf{w}}^{t-1}$ prompt for the current mini-batch, minimising the impact of model parameter distribution drift on the $\hat{\mathbf{w}}^{t-1}$ prompt.

This is important as a radiologist report may not always be available for the previous study in practice. When testing, the difference in performance between \mathbf{w}^{t-1} and $\hat{\mathbf{w}}^{t-1}$ as the prompt can reveal how errors introduced in $\hat{\mathbf{w}}^{t-1}$ impact report generation.

3.3. CXR-BERT Cosine Similarity Reward

CXR-BERT is a Transformer encoder pre-trained in various stages on PubMed abstracts, clinical notes from MIMIC-III (Johnson *et al.*, 2016), as well as reports from MIMIC-CXR, which we denote as $E(\cdot)$ (Boecking *et al.*, 2022). It has two pre-training tasks, with one being Radiology Section Matching (RSM). For RSM, the output feature vector for the [CLS] special token of CXR-BERT ($[E(\cdot)]_{[CLS]}$) and a two-layer feed-forward neural network ($P(\cdot)$) are used in series to compute features of the findings and impression sections. During RSM, a contrastive loss forces the findings and impression section features from the same report to have a higher similarity, while forcing those from different reports to have a lower similarity.

We leverage CXR-BERT as a reward for SCST, as shown in Figure 4. Instead of sections, we compute the similarity between the generated and radiologist reports (which include both the findings and impression sections). Features for the generated and radiologist reports are first computed as: $\hat{\mathbf{t}} = P([E(\hat{\mathbf{w}}^t)]_{[CLS]})$ and $\mathbf{t} = P([E(\mathbf{w}^t)]_{[CLS]})$, respectively. Their cosine similarity then gives the reward: $r = (\hat{\mathbf{t}} \cdot \mathbf{t}) / (\|\hat{\mathbf{t}}\| \cdot \|\mathbf{t}\|)$. Generated and radiologist reports that are semantically similar will have a higher cosine similarity, while semantically dissimilar reports will have a lower cosine similarity. With this as the reward for SCST, the model will learn to generate reports that are semantically similar to radiologist reports.

3.4. Section Embeddings and Issues With Labels in the Literature

Two additional factors can impact the performance of a CXR report generator, and these pertain to the labels used to develop and evaluate a CXR report generator. The first is that a radiologist’s interpretation of a patients study is typically authored in multiple sections in a radiology report, including but not limited to a *findings* section (which details the interpretation of a study) and an *impression* section (which summarises the most important findings). However, current models are either only evaluated with labels that include only one of these sections (Chen *et al.*, 2020), or they often do not differentiate between these sections during generation (Thawkar *et al.*, 2023). Only the findings section is considered in the labels of Chen *et al.* (2020), which are frequently used in the literature (an example is shown in Table 1). To account for the different sections, we introduce a separator token into the report generation process

that allows the findings and impression sections of the generated report to be recovered. Moreover, we differentiate each of the sections of the report to the decoder with section embeddings — a non-standard practice for Transformer decoders borrowed from pre-trained Transformer encoders (Devlin *et al.*, 2019).

The second aspect is formatting that alters or removes information from the radiology reports. For example, the formatting used to form the labels of Chen *et al.* (2020) truncates 10% of the findings sections from the MIMIC-CXR test set (by having a maximum of 100 tokens per label). An example of the information loss that this can cause is shown in Table 2; multiple important findings are lost due to the truncation. Instead, we minimise information loss by setting a maximum of 256 tokens for our labels (which includes both the findings and impression sections), which results in only 0.3% of the reports from the test set being truncated. While this is at the cost of computational complexity, less information is lost from the original reports. Note that we only truncate the radiologist reports to 256 tokens during training; we do not truncate the radiologist reports during validation or testing.

By excessively formatting the radiologist reports and not considering the impression section, the fidelity of the labels of Chen *et al.* (2020) to the findings and impressions of the radiologists is weakened. This leads to an artificial evaluation setting which has permeated through the field of CXR report generation, as many models in the literature have been evaluated with the labels of Chen *et al.* (2020).

3.5. Experiment Setup

3.5.1. Dataset

The MIMIC-CXR dataset was used for model training and evaluation (Johnson *et al.*, 2019), while the IU X-ray dataset was used solely for evaluation (Demner-Fushman *et al.*, 2016). The use of human data provided in these datasets was approved by the CSIRO Health and Medical Human Research Ethics Committee (2019_086_LR).

Currently, MIMIC-CXR is the sole publicly-available dataset to retain longitudinal information between studies. Sections from the radiologist reports of MIMIC-CXR were obtained using the official text extraction tool.² Studies with either a missing findings or impression section, and studies with more than five CXRs per study were removed from the official training/validation/test split. This gave a split of 57 098/436/280 patients, 125 395/991/1 624 studies, and 232 715/1 837/2 872 CXRs. Minimal formatting was applied to the radiologist reports; newline and tab characters were removed, and consecutive white spaces were replaced with a single white-space character. The order of a patient’s studies was determined by the date and time provided with the metadata. The date and time for studies 57077869 and 58837588 of patient 15964158 were identical, making it impossible to determine their order. Hence, these studies, along with all of their subsequent studies were removed from the training set for the longitudinal case only,

²<https://github.com/MIT-LCP/mimic-cxr/tree/master/txt>

Table 1. An example label from Chen *et al.* (2020); the impression section is not included. The missing impression section from the original report is highlighted.

Issue	Label from Chen et al. (2020)	Original findings & impression sections
No impression section (study_id: 59542064).	Findings: the heart size appears moderately enlarged . the mediastinum demonstrates tortuosity of the thoracic aorta . there is perihilar haziness with vascular indistinctness compatible with mild pulmonary edema . hazy opacities in both lung bases likely reflect small layering bilateral pleural effusions with associated bibasilar atelectasis . no large pneumothorax is identified . there are no acute osseous abnormalities .	Findings: The heart size appears moderately enlarged. The mediastinum demonstrates tortuosity of the thoracic aorta. There is perihilar haziness with vascular indistinctness, compatible with mild pulmonary edema. Hazy opacities in both lung bases likely reflect small layering bilateral pleural effusions with associated bibasilar atelectasis. No large pneumothorax is identified. There are no acute osseous abnormalities. Impression: Mild pulmonary edema with small bilateral pleural effusions and bibasilar atelectasis.

Table 2. An example label from Chen *et al.* (2020). The truncation used to form the label results in information loss from the original findings section. The missing part of the findings section from the original report is highlighted.

Issue	Label from Chen et al. (2020)	Original findings & impression sections
Information loss; truncation after the 100th token (study_id: 55420918).	Findings: the heart is mildly enlarged with a left ventricular configuration . there is similar unfolding of the thoracic aorta . the mediastinal and hilar contours appear unchanged including a convexity along the right upper mediastinal contour . particularly since it appears stable over time it can probably be attributed to tortuosity of the great vessels . at both lung bases but more extensive on the right than left there are patchy opacities fairly streaky in nature but extensive . these are increased since the earlier examination and are accompanied by peribronchial cuffing . there is no pleural effusion or	Findings: The heart is mildly enlarged with a left ventricular configuration. There is similar unfolding of the thoracic aorta. The mediastinal and hilar contours appear unchanged including a convexity along the right upper mediastinal contour. Particularly since it appears stable over time, it can probably be attributed to tortuosity of the great vessels. At both lung bases, but more extensive on the right than left, there are patchy opacities, fairly streaky in nature but extensive. These are increased since the earlier examination and are accompanied by peribronchial cuffing. There is no pleural effusion or pneumothorax. Suspected mild loss in mid thoracic vertebral body heights appears unchanged and probably coincides with demineralization. The lower thoracic spine shows mild rightward convex curvature. There is wedging of an upper lumbar vertebral body which may be increased somewhat, although the apparent difference may be due to differences in orientation. Impression: 1. Increasing bibasilar opacities which could be seen with lower airway inflammation or infection, although developing bronchopneumonia is not entirely excluded. 2. Mild anterior wedge compression deformity of a vertebral body at the thoracolumbar junction, likely L1; although probably chronic, potentially increased somewhat.

reducing the training set size to 125 384 studies and 232 692 CXRs.

For IU X-ray, we use the entire dataset as a test set to evaluate the generalisability of the models trained on MIMIC-CXR. Findings and impression sections were extracted for each study from their corresponding XML file, where studies that did not include both a findings and impression section were excluded. No formatting was applied to either section. Longitudinal data for IU X-ray could not be leveraged as only one study per patient is available. With each study including one or more CXRs, the test set consisted of 3 331 studies and 6 461 CXRs.

For MIMIC-CXR, we use the JPG version (MIMIC-CXR-JPG). Similarly, for IU X-ray, we use the PNG version. This is standard in the literature for CXR report generation, where the DICOM versions of both datasets are avoided. This is not ideal, as fidelity is lost to the DICOMs. To form the JPG and PNG versions of the datasets, the authors first reduced the pixel bit depth of the DICOMs from 12-16 bits to 8 bits. Furthermore, the JPG format is lossy. These factors increase the quantisation error to the DICOMs, which could be detrimental for CXR report generation. We discuss this further in Section 5.

3.5.2. Model

CvT was the encoder (specifically, CvT-21 pre-trained on ImageNet-22K and fine-tuned on ImageNet-1K at a resolution of 384×384) (Wu *et al.*, 2021). Layer normalisation was applied to its last hidden state, followed by a projection to the decoder’s hidden size. The encoded features for each image of a study were concatenated and fed to the cross-attention of the decoder. Each image was resized using bilinear interpolation so that its smallest side had a length of 384 and its largest side maintained the aspect ratio. Next, the resized image was cropped to a size of $\mathbb{R}^{3 \times 384 \times 384}$. The crop location was random during training and centred during testing. Following Elgendi *et al.* (2021), the image was rotated around its centre during training, where the angle of rotation was sampled from $\mathcal{U}[-5^\circ, 5^\circ]$. Finally, the CXR was standardised using the statistics provided with the CvT-21 checkpoint.

For the decoder, a byte-level byte pair encoding tokeniser (Wang *et al.*, 2020) was trained on the findings and impression sections of the training set (with a vocabulary size of 30 000). Tokens were fed to a randomly-initialised Transformer decoder with six layers and a language model head with a vocabulary size of 30 000. For the longitudinal, multi-image case, we found that training the described model on the longitudinal, multi-image CXR report generation task would not result in an improvement over the multi-image case. To ease the difficulty of learning this task, we adapt a trained multi-image CXR model to the task of longitudinal, multi-image CXR report generation using Low-Rank Adaptation (LoRA) (Hu *et al.*, 2022). LoRA is applied to the query and key weights of each self-attention head of the decoder with a rank of eight, an alpha of 32, and a dropout rate of 0.1. LoRA adds 147K parameters to the 80.8M parameters of the encoder-to-decoder model, where all non-LoRA parameters are frozen during fine-tuning. Greedy search and beam search with four beams were employed during validation and testing, respectively.

3.5.3. Training

Two stages of training were performed; teacher forcing, followed by SCST. *AdamW* (Loshchilov and Hutter, 2022) was used for mini-batch gradient descent optimisation at an initial learning rate of 5e-5 for teacher forcing and 5e-6 for SCST, with a mini-batch size of 32, for 32 epochs with teacher forcing, and for 1 epoch with SCST on 4×16 GB NVIDIA Tesla P100 GPUs. For SCST, validation was performed every $\frac{1}{10}$ of an epoch. The validation macro-averaged CheXbert F1 was the monitored metric for checkpoint selection. For SCST, the baseline was generated with greedy search, while the sample was produced with top- k sampling ($k = 50$). During SCST, the encoder was frozen, while all parameters of the decoder were learnable (both LoRA and non-LoRA parameters). The maximum number of tokens for the generated report and the prompt was 256 each.

3.5.4. Comparison Models and Rewards

We compared the CXR-BERT reward to other rewards, including CIDEr (Vedantam *et al.*, 2015), Clinical Correctness Reward (CCR) (with CheXbert instead of the CheXpert labeller Irvin *et al.* (2019)) (Liu *et al.*, 2019), fact_{ENTNLI} and fact_{ENTNLI} + BERTScore (Miura *et al.*, 2021), as well as RadGraph ER (Delbrouck *et al.*, 2022). Moreover, we compared our CXR report generator to others in the literature that had available code and model checkpoints. These included R2Gen (Chen *et al.*, 2020), \mathcal{M}^2 fact_{ENT} and \mathcal{M}^2 fact_{ENTNLI} (Miura *et al.*, 2021), WCL (Yan *et al.*, 2021), CMN (Chen *et al.*, 2021), and CvT2DistilGPT2 (Nicolson *et al.*, 2023). We also compared to Med-Flamingo with the following prompt for few-shot learning (Moor *et al.*, 2023):

<image> F_1 <|endofchunk|><image> F_2 <|endofchunk|>
<image> F_3 <|endofchunk|><image> F_4 <|endofchunk|>
<image> F_5 <|endofchunk|><image>. Five random CXRs were selected from the training set for the prompt, along with their corresponding findings sections (F_1 to F_5). For LLaVA-Med, ‘Describe the following image in detail.’ was used to instruct LLaVA-Med, following Li *et al.* (2023, Table 8). Scores for UniXGen (Lee *et al.*, 2023), XrayGPT (Thawkar *et al.*, 2023), LLM-CXR (Lee *et al.*, 2024), and MedXChat (Yang *et al.*, 2023) were quoted from Yang *et al.* (2023), as either their code or model checkpoint was unavailable. Each model checkpoint was trained on MIMIC-CXR, and not IU X-ray.

3.5.5. Metrics

CheXbert (Smit *et al.*, 2020), RadGraph ER, BLEU (Papineni *et al.*, 2001), and BERTScore F1³ (Zhang *et al.*, 2020) have been found to correlate with radiologists’ assessment of reporting (Yu *et al.*, 2023) and were a part of our evaluation. Additionally, we include CIDEr (Vedantam *et al.*, 2015) and ROUGE-L (Lin and Hovy, 2003), and propose to use the CXR-BERT cosine similarity as a metric. CheXbert, RadGraph ER, and CXR-BERT were intended to capture the clinical semantic similarity between the generated and radiologist reports, while

³roberta-large_L17_no-idf_v=0.3.12(hf=4.25.1)-rescaled

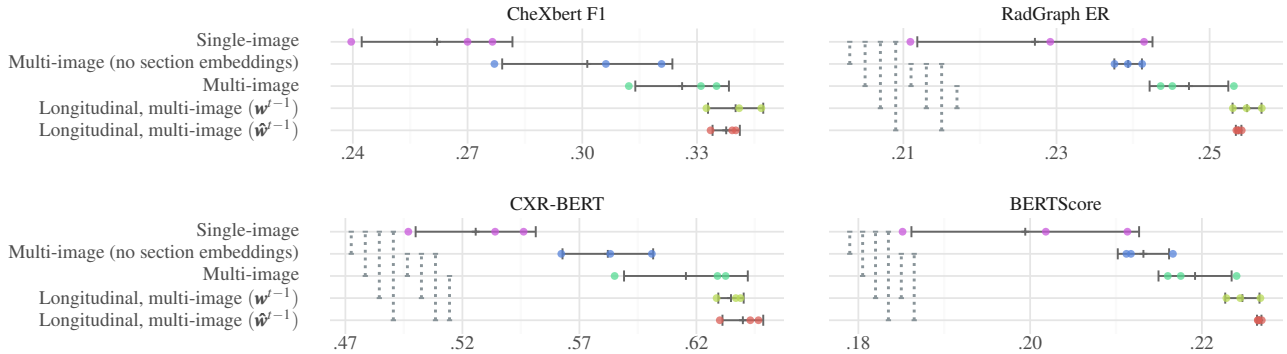


Fig. 5. Results for the different conditioning strategies of Figure 2. The error bars indicate the mean and standard deviation over three training runs. Dotted lines indicate a significant difference between the scores of two methods ($p < 0.05, n = 4872; 1624$ studies $\times 3$ runs). w^{t-1} indicates the radiologist report as the prompt, while \hat{w}^{t-1} indicates the generated report as the prompt.

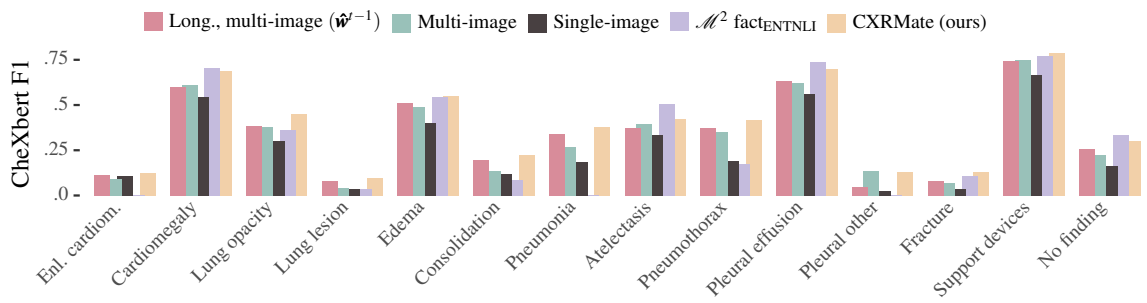


Fig. 6. F1 for each CheXbert observation ($n = 1624$ studies).

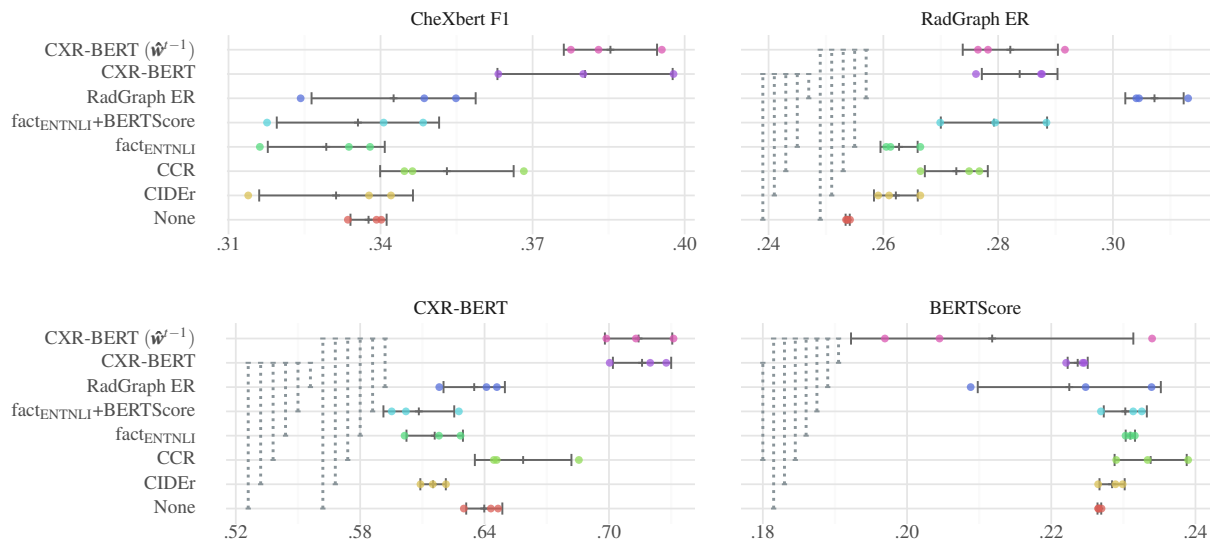


Fig. 7. Results for each reward with the longitudinal, multi-image CXR report generator. The error bars indicate the mean and standard deviation over three training runs. Dotted lines indicate a significant difference between the scores of a method and CXR-BERT ($p < 0.05, n = 4872; 1624$ studies $\times 3$ runs).

Table 3. Scores of the generated findings sections (versus the findings sections from the radiologist reports) on the MIMIC-CXR test set ($n = 1,624$ studies). Each model was implemented using available code repositories and model checkpoints.

Model	Multi-image	CheXbert			RadGraph ER	CXR-BERT	BERTSc.	CIDEr	ROUGE-L	BLEU-4
		F1	P	R						
<i>Biomedical Image VQA Models</i>										
Med-Flamingo few-shot	✗	0.001	0.051	0.000	0.210	-0.175	0.269	0.042	0.192	0.027
LLaVA-Med	✗	0.142	0.202	0.127	0.049	0.109	0.000	0.011	0.134	0.001
<i>CXR report generators</i>										
R2Gen	✗	0.160	0.360	0.151	0.204	0.377	0.195	0.113	0.235	0.056
WCL	✗	0.208	0.327	0.199	0.211	0.459	0.195	0.116	0.234	0.055
CMN	✗	0.251	0.353	0.250	0.224	0.482	0.213	0.134	0.240	0.058
CvT2DistilGPT2	✗	0.258	0.414	0.249	0.226	0.596	0.214	0.165	0.245	0.064
M^2 factENT	✓	0.235	0.381	0.244	0.237	0.553	0.216	0.133	0.207	0.060
M^2 factENTNLI	✓	0.311	0.412	0.329	0.320	0.681	0.289	0.187	0.269	0.083
CXRMate (ours)	✓	0.357	0.438	0.349	0.272	0.700	0.280	0.205	0.262	0.079

BERTscore was intended to capture general semantic similarity. Finally, CIDEr, ROUGE-L, and BLEU-4 were intended to capture the syntactic similarity between the generated and radiologist reports. For the single-image models, we average the scores over all reports for a study. Following this, the average was taken over the scores for all studies for single- and multi-image models.

For CheXbert, the macro-averaged F1, Precision (P), and Recall (R) were computed between the 14 CheXbert observations extracted from the generated and radiologist reports. “No mention”, “negative”, and “uncertain” were considered negative, while “positive” was considered positive. Here, the true positives, false positives, and false negatives were averaged over the reports of each study for the single-image case. We also perform statistical testing; first, a Levene’s test revealed that the variances across models were not homogeneous. Next, a one-way Welch’s ANOVA determined that there was a significant difference between models. Finally, Games-Howell post hoc tests were used for pairwise testing. Statistical testing was not performed for CheXbert, as it is a binary classification-based metric.

4. Results & Discussion

4.1. Single, Multi, & Longitudinal Conditioning

First, we discuss the results for single-image, multi-image, and longitudinal, multi-image CXR report generation (where each was trained with teacher forcing). The multi-image case significantly outperformed the single-image case on all metrics in Figure 5 and achieved a higher F1 on 13 of the 14 CheXbert observations in Figure 6. This indicates that conditioning on all CXRs of a study (which may contain both frontal and lateral views) improves CXR report generation. This aligns with the radiologist workflow, as certain abnormalities are more easily identifiable with both views (Gaber *et al.*, 2005).

Longitudinal, multi-image CXR report generation outperformed the multi- and single-image cases on all metrics in Figure 5 and on 10 of the 14 CheXbert observations in Figure 6. Moreover, the difference between prompting with \mathbf{w}^{t-1} and $\hat{\mathbf{w}}^{t-1}$ was not statistically significant, indicating that conditioning on a generated report from the previous study rather than the radiologist’s report from the previous study does not hinder generation. The results indicate that conditioning on longitudinal data

improves CXR report generation and diagnostic accuracy. This aligns with the radiologist workflow, as diagnostic accuracy can improve when the previous study is available for comparison (Kelly, 2012).

Figure 5 also shows that section embeddings improve the scores on each metric (when looking at the multi-image case, with and without section embeddings).⁴ There was little difference between the distribution of each section’s vocabulary, with a Kullback–Leibler divergence of 0.04 between the findings and impression section token distributions on the training set. Yet, the findings sections are 3.4 times longer on average than the impression sections. Such a difference in length is indicative of the purpose of the impression section: to summarise the findings. We hypothesise that signalling to the decoder which section the next token belongs to via section embeddings may allow it to better understand which task it must perform: interpretation or summarisation.

4.2. Rewards for Reinforcement Learning

The results for each reward used with SCST — a reinforcement learning algorithm — are given in Figure 7. Each reward was evaluated using the longitudinal, multi-image CXR report generator prompted with \mathbf{w}^{t-1} during training and testing, except for CXR-BERT ($\hat{\mathbf{w}}^{t-1}$) (which was prompted with $\hat{\mathbf{w}}^{t-1}$ during training and testing). As expected, CXR-BERT and RadGraph ER each performed best on the corresponding metrics that they were optimised on (CXR-BERT and RadGraph ER, respectively). Yet, CXR-BERT attained the highest CheXbert F1, indicating that rewarding based on similar latent alignments with CXR-BERT is a promising alternative to rewarding based on matching entities and relations with RadGraph ER. Comparing CXR-BERT (which was prompted with \mathbf{w}^{t-1}) to CXR-BERT ($\hat{\mathbf{w}}^{t-1}$), their performance was similar, indicating that any errors in $\hat{\mathbf{w}}^{t-1}$ had no significant impact on performance. We note that the CXR-BERT reward moderately increased repetitions in the generated reports for some training runs (likely causing the low BERTScores).

⁴Each model in Figure 5 uses section embeddings, except ‘Multi-image (no section embeddings)’.

Table 4. Differences between the test sets and the labels of each model. Details are sourced from the respective paper of each model.

Model	Test set	Sections	Formatting	Multi-image
UniXGen	4 444 images and 2 733 studies from the MIMIC-CXR test set.	Findings and impression.	Lowercase.	✓
XrayGPT	MIMIC-CXR test set, exclusion schema unknown.	Combined the findings and impression sections.	Unknown.	✗
LLM-CXR	3 530 images; lateral views were excluded from the MIMIC-CXR test set.	Impression.	Unknown.	✗
MedXChat	3 858 images; studies without a findings section were excluded from the MIMIC-CXR test set.	Findings and impression.	Followed the formatting of Chen et al. (2020), differing by applying it also to the impression section.	✗
CXRMate (ours)	2 872 images, 1 624 studies, and 280 patients; studies without a findings or impression section, or more than five images were excluded from the MIMIC-CXR test set.	Findings and impression.	Newline characters, tab characters, and consecutive white spaces were replaced with a single white-space character.	✓

Table 5. CheXpert F1 scores on the MIMIC-CXR test set for the generated reports. We use CheXbert to estimate the CheXpert observations for our model (Irvin et al., 2019). † indicates results quoted from Yang et al. (2023). Following Yang et al. (2023), the logical disjunction (OR) was taken between the consolidation and pneumonia observations. F and I indicate the findings and impression sections, respectively.

	UniXGen-256 [†]	XrayGPT [†]	LLM-CXR [†]	MedXChat [†]	CXRMate (ours)
Sections	F & I	F + I	I	F & I	F & I
Multi-image	✓	✗	✗	✗	✓
Micro	0.281	0.314	0.414	0.420	0.529
Macro	0.187	0.227	0.283	0.292	0.378
No Findings	0.411	0.371	0.562	0.318	0.280
Pneumothorax	0.083	0.049	0.083	0.092	0.388
Edema	0.226	0.333	0.370	0.398	0.552
Effusion	0.215	0.404	0.455	0.718	0.671
Consolidation OR Pneumonia	0.132	0.143	0.198	0.177	0.380
Lung lesion	0.055	0.058	0.030	0.049	0.067

Table 6. Natural language generation metric scores on the MIMIC-CXR test set for the generated reports. † indicates results quoted from Yang et al. (2023). F and I indicate the findings and impression sections, respectively.

Model	Multi-image	Sections	BLEU-4	ROUGE-L	METEOR	CIDEr
UniXGen-256 [†]	✓	F & I	0.101	0.294	0.156	0.138
LLM-CXR [†]	✗	I	0.033	0.245	0.081	0.445
MedXChat [†]	✗	F & I	0.111	0.264	0.135	0.175
CXRMate (ours)	✓	F & I	0.074	0.255	0.158	0.172

4.3. Comparison to Other Models

In Table 3, our longitudinal, multi-image CXR report generator + CXR-BERT reward (prompted with \hat{w}^{t-1} during training and testing), which we name CXRMate, was compared to other models in the literature. Note that while CXRMate generates both the findings and impression sections, the remaining models in Table 3 generate only the findings section. Therefore, only the findings section for CXRMate was evaluated in Table 3 (against the findings section from the radiologist reports), and the impression section was ignored.

CXRMate produced the highest CheXbert (F1, P, and R), CXR-BERT, and CIDEr scores. \mathcal{M}^2 fact_{ENTNLI} is conditioned on all CXRs of a study, and was trained with a composite reward; it represents a strong benchmark. The superior performance of \mathcal{M}^2 fact_{ENTNLI} on RadGraph ER and BERTScore is likely due to it being optimised with its fact_{ENTNLI} and BERTScore reward, where fact_{ENTNLI} is an NER-based reward that is similar to RadGraph ER. CXRMate outperformed \mathcal{M}^2 fact_{ENTNLI} on 10 out of the 14 CheXbert observations in Figure 6. While \mathcal{M}^2 fact_{ENTNLI} performed well for *cardiomegaly*, *atelectasis*, and *pleural effusion*, it failed to correctly detect *enlarged cardiomedastinum* or *pleural other* throughout the entire test set. CXRMate also performed best for lung lesion, a difficult and important abnormality to detect, made more difficult by the fact that it is underrepresented in the MIMIC-CXR training set (Johnson *et al.*, 2019, Table 2). These results indicate that CXRMate was able to generate reports that are quantitatively more aligned with those of radiologists than previous models (in terms of the CheXbert, CXR-BERT, and CIDEr scores).

The low performance of R2Gen, WCL, CMN, and CvT2DistilGPT2 could be attributed to being conditioned on a single-image, not leveraging longitudinal data, not being trained with SCST, and being trained on the truncated labels of Chen *et al.* (2020) (described in Table 2). Moreover, the results indicate that the the biomedical image VQA models, namely Med-Flamingo and LLaVA-Med, struggled to interpret the CXRs. Furthermore, Med-Flamingo struggled to adapt to the task, even though it was prompted with five examples for few-shot learning.

4.4. Comparison to Multi-Task Learning models

Here, we test against the multi-task learning models presented in Table 4, of which XrayGPT, LLM-CXR, and MedX-Chat leverage LLMs. We compare to the results from Yang *et al.* (2023), due to lack of code and model availability. First, in Table 4 we highlight the discrepancies between each of the models evaluated in Yang *et al.* (2023). Each splits the MIMIC-CXR test set differently, with some excluding based on missing sections, and others excluding based on the view of the image. Moreover, there were differences between how the findings and impression sections are treated. Some only used one section, others combined the sections, and some differentiated between the sections. Each also formatted the radiologist reports differently, with some having unclear formatting rules. And finally, some were single-image models, and generated a report per image, while others were multi-image models, and generated a report per study.

Given these discrepancies, claims made from a comparison between these models will be weak. Nevertheless, we compare to these multi-task learners in Tables 5 and 6. Here, F + I indicates that the findings and impression sections were combined, while F & I indicates that the sections could be differentiated after generation. CXRMate attained the highest micro and macro-averaged CheXpert F1 scores in Table 5, as well as the highest scores for *pneumothorax*, *edema*, *consolidation* or *pneumonia*, and *lung lesion*. This weakly indicates that CXRMate is more diagnostically accurate than the multi-task learning models. Each model in Table 6 attained the highest score for one metric, likely due to the discrepancies between the evaluation procedures of each model.

4.5. Generalisability to the IU X-ray dataset

Here, we assess the generalisability of CXRMate, which has been trained on MIMIC-CXR, to another dataset, specifically, IU X-ray. Currently, the only publicly-available dataset where longitudinal data can be leveraged is MIMIC-CXR. IU X-ray only includes one study per patient, preventing longitudinal data from being leveraged. This is disadvantageous for CXRMate, as it cannot condition on the report from the previous study. Nevertheless, we evaluate the performance of CXRMate on IU X-ray, as shown in Table 7. CXRMate generates both the findings and impression sections, while the remaining models in Table 7 generate only the findings section. Therefore, only the findings section for CXRMate was evaluated in Table 7 (against the findings section from the radiologist reports), and the impression section was ignored.

CXRMate produced the highest CheXbert (F1 and R) and CXR-BERT scores, indicating that it was able to generalise well in terms of clinical semantic similarity to the radiologist reports. However, \mathcal{M}^2 fact_{ENTNLI} and \mathcal{M}^2 fact_{ENT} attained a higher BERTScore, CIDEr, ROUGE-L, and BLEU-4, indicating that CXRMate was not able to generalise as well in terms of general semantic and syntactical similarity to the radiologist reports. This may have been exacerbated by the unavailability of the previous studies during generation. While \mathcal{M}^2 fact_{ENTNLI} attained the highest BERTScore and ROUGE-L scores, \mathcal{M}^2 fact_{ENT} attained the highest RadGraph ER, CIDEr, and BLEU-4 scores. Previously, in Table 3, \mathcal{M}^2 fact_{ENTNLI} outperformed \mathcal{M}^2 fact_{ENT} on each metric with the MIMIC-CXR test set. This indicates that \mathcal{M}^2 fact_{ENT} was able to better generalise from the MIMIC-CXR test set to the IU X-ray dataset than \mathcal{M}^2 fact_{ENTNLI}.

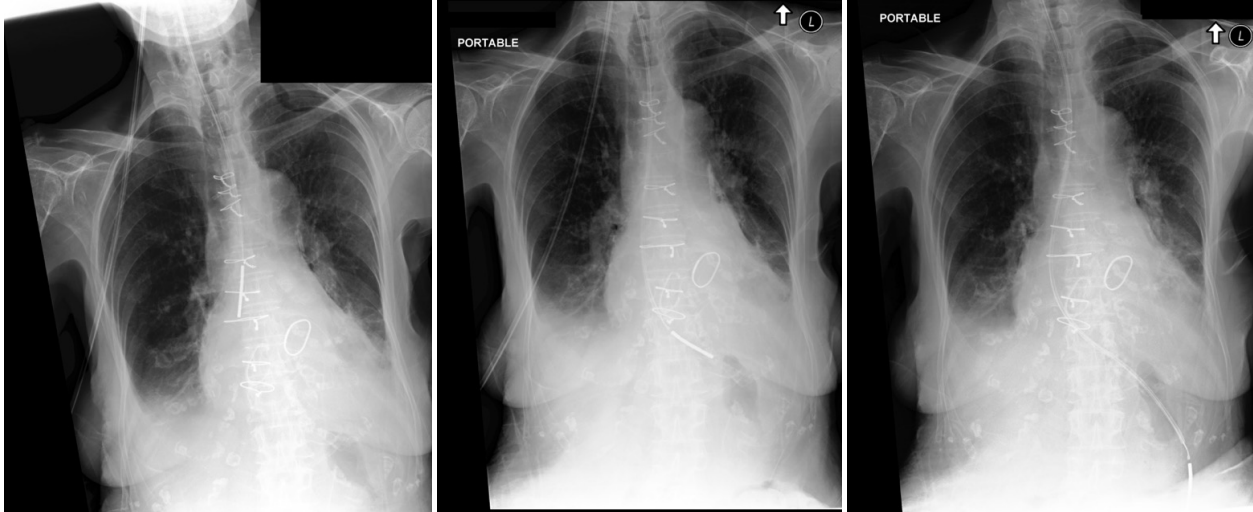
4.6. Case Studies

In Table 8, we show a study where CXRMate attained a high CheXbert F1 score. The study is of a feeding tube being inserted into the stomach. It includes three CXRs and is an example of why it is important to condition on all images of a study, even if they are all the same view. Along with the feeding tube, this study includes postoperative hardware, mitral and tricuspid heart valve replacements, and several pathologies. CXRMate successfully identified most of these (minus the tricuspid heart valve replacement). \mathcal{M}^2 fact_{ENTNLI} was only able to identify the feeding tube, the small bilateral pleural effusions, and the

Table 7. Scores of the generated findings sections (versus the findings sections from the radiologist reports) on the IU X-ray dataset ($n = 3331$ studies). Each model was implemented using available code repositories and model checkpoints, and was trained on the MIMIC-CXR dataset, not the IU X-ray dataset. * indicates that the model was not conditioned on the report from the previous study, as the previous study is not available with the IU X-ray dataset.

Model	Multi-image	CheXbert			RadGraph-ER	CXR-BERT	BERTSc.	CIDEr	ROUGE-L	BLEU-4
		F1	P	R						
R2Gen	✗	0.102	0.195	0.101	0.210	0.544	0.190	0.078	0.213	0.023
WCL	✗	0.143	0.161	0.167	0.214	0.555	0.194	0.077	0.213	0.022
CvT2DistilGPT2	✗	0.220	0.381	0.214	0.258	0.589	0.253	0.141	0.255	0.039
M^2 fact _{ENT}	✓	0.210	0.275	0.265	0.366	0.558	0.353	0.252	0.314	0.068
M^2 fact _{ENTNL}	✓	0.234	0.354	0.256	0.334	0.620	0.359	0.239	0.316	0.066
CXRMate (ours)*	✓	0.277	0.351	0.283	0.291	0.683	0.323	0.164	0.282	0.046

Table 8. A study where CXRMate attained a high CheXbert score. Shown are the three CXRs included with the study, along with a radiologist's report and generated reports. Matching highlighting indicates true positive observations between the generated and radiologist's report. The report generated by CXRMate was the most similar to the radiologist's report and only failed to detect the tricuspid heart valve replacement. The CheXbert score was calculated between the findings sections only.



Radiologist's report (study 59144799 of patient 18224196. Their previous study (53536595) was 59 hours prior.)

Findings: Feeding tube tip in the distal stomach. Central line, endotracheal tube have been removed. Sternotomy, valve replacements. Small bilateral pleural effusions have worsened. Left basilar atelectasis or infiltrate, worsened. Right basilar atelectasis, worsened. Increased heart size, more prominent. Mildly prominent pulmonary vascularity.

Impression: Feeding tube tip in the distal stomach. Worsened pulmonary findings

CXRMate (ours) *CheXbert F1 score: 1.000*

Findings: The patient is status post median sternotomy and mitral valve replacement. A Dobhoff tube terminates in the stomach. There are small to moderate bilateral pleural effusions with subjacent atelectasis. The heart is mildly enlarged. There is mild pulmonary vascular congestion. No pneumothorax is identified. There are no acute osseous abnormalities.

Impression: The Dobhoff tube terminates in the stomach. Small to moderate bilateral pleural effusions with subjacent atelectasis. Mild pulmonary vascular congestion.

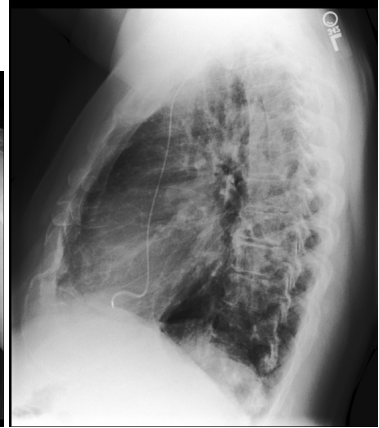
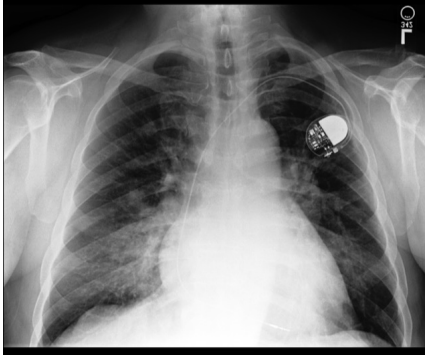
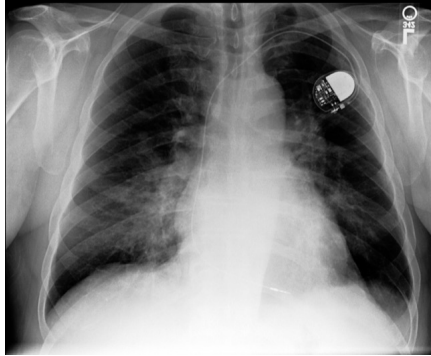
M^2 fact_{ENTNL} *CheXbert F1 score: 0.857*

Findings: the cardiomedastinal and hilar contours are stable . the nasogastric tube ends in the stomach . the lung volumes are lower compared to the prior chest radiograph . small bilateral pleural effusions are unchanged . small right pleural effusion is unchanged . there is bibasilar atelectasis . there is no pneumothorax . a dobbhoff tube is seen with the tip in the stomach .

CvT2DistilGPT2 *CheXbert F1 score: 0.333*

Findings: as compared to the previous radiograph the patient has received a dobbhoff catheter. the course of the catheter is unremarkable the tip of the catheter projects over the middle parts of the stomach. there is no evidence of complications notably no pneumothorax. otherwise the radiograph is unchanged.

Table 9. A study where CXRMate attains a low CheXbert score. Shown are the three CXRs included with the study, along with a radiologist's report and generated reports. Matching highlighting indicates true positive observations between the generated and radiologist's report. The CheXbert score was calculated between the findings sections only.



Radiologist's report (*study 59698565 of patient 18570152. There was no prior study available.*)

Findings: Frontal and lateral views of the chest are obtained. Right lower lobe opacity is worrisome for consolidation, possibly due to pneumonia. Along the superior aspect of the right lower lung consolidation, there is a 0.9-cm nodular opacity, projecting between the posterior right sixth and seventh ribs, which could relate to consolidation or an underlying pulmonary nodule is not excluded. Recommend followup chest radiograph after appropriate therapy and if finding remains, chest CT. There is also a left suprahilar opacity, which could be a second site of infection or relate to mild volume overload. There is central pulmonary vascular engorgement. No large pleural effusion or pneumothorax is seen. Single-lead left-sided pacemaker is seen with leads in the expected position of the right ventricle. The cardiac silhouette is enlarged.

Impression: Right lower lobe and left infrahilar opacities, right greater than left, in the appropriate clinical setting, raises concern for pneumonia. Recommend followup to resolution. Possible 0.9 cm nodular opacity along the superior aspect of the right lower lung opacity, could relate to consolidation, but pulmonary nodule not excluded. Recommend followup chest radiographs after appropriate therapy and if finding remains, chest CT. Left suprahilar opacity, which could be a second site of infection or relate to mild volume overload. Pulmonary vascular engorgement. Enlarged cardiac silhouette.

CXRMate (ours) *CheXbert F1 score: 0.333*

Findings: Frontal and lateral views of the chest were obtained. There is new right middle lobe consolidation worrisome for pneumonia. The left lung is clear. There is no pleural effusion or pneumothorax. The cardiac and mediastinal silhouettes are stable. Single lead left-sided pacemaker is seen with lead extending to the expected position of the right ventricle.

Impression: Right middle lobe consolidation worrisome for pneumonia. Recommend followup to resolution.

M^2 fact_{ENTNLI} *CheXbert F1 score: 0.333*

Findings: the cardiomedastinal and hilar contours are normal. the heart is mildly enlarged. the lung volumes are lower compared to the prior chest radiograph. there is mild pulmonary edema. there is no focal consolidation. no pleural effusion or pneumothorax is seen. a left chest pacemaker is seen with leads in the right atrium and right ventricle.

CvT2DistilGPT2 *CheXbert F1 score: 0.400*

Findings: frontal and lateral views of the chest were obtained. single-lead left-sided pacemaker is again seen with lead extending to the expected position of the right ventricle. bilateral perihilar opacities right greater than left are worrisome for multifocal pneumonia. no pleural effusion or pneumothorax is seen. cardiac and mediastinal silhouettes are stable.

Table 10. A study highlighting the issues introduced by the labels of Chen *et al.* (2020). Shown is a CXR from a study, along with a radiologist's report and generated reports. Matching highlighting indicates true positive observations between the generated and radiologist's report. The CheXbert score was calculated between the findings sections only.



Radiologist's report (study 54849848 of patient 10886362. Their previous study (56034024) was 3 days and 21 hours prior.)

Findings: AP single view of the chest has been obtained with patient in sitting semi-upright position. Comparison is made with the next preceding portable chest examination with the patient in supine position as of _____. Again noted is status post sternotomy and significant enlargement of the cardiac silhouette. Previously described permanent pacer in left axillary position with two intracavitory electrodes in unchanged location. Unchanged position of left internal jugular approach central venous line terminating in upper portion of SVC. No pneumothorax has developed. Diffuse haze over both lung bases as before obliterating the diaphragmatic contours and indicative of bilateral pleural effusions partially layering posteriorly. The pulmonary venous congestive pattern persists. An intra-aortic balloon pump device is seen to terminate in the descending thoracic aorta about 3 cm below the level of the lower thoracic arch contour. This is unchanged.

Impression: No significant interval changes during the last 24 hours interval. The described changes with postoperative status, CHF, pleural effusion and intra-aortic balloon pump device in place is of course compatible with the patient's hypoxia.

CXRMat (ours) *CheXbert F1 score: 0.75*

Findings: AP single view of the chest has been obtained with patient in semi-upright position. The patient is now intubated, the ETT terminating in the trachea 5 cm above the level of the carina. A right internal jugular approach central venous line is seen to terminate in the mid portion of the SVC. A left internal jugular approach central venous line remains in unchanged position terminating in the mid portion of the SVC. An NG tube has been passed and reaches below the diaphragm, and terminates in the fundus of the stomach with side port remaining in the distal esophagus. The patient is status post sternotomy, CABG, and mitral valve prosthesis. The heart is mildly enlarged and the pulmonary vasculature is not congested. There are bilateral pleural effusions, slightly more so on the right than the left. There is no pneumothorax and no new parenchymal opacities are present in the apical area.

Impression: NG tube reaches below the diaphragm, and side port is in the distal esophagus. Post-CABG changes. Bilateral pleural effusions, slightly larger on the right than the left and mild on the right, and mild on the left, are stable.

CvT2DistilGPT2 *CheXbert F1 score: 0.286*

Findings: as compared to the previous radiograph the patient has been intubated. the tip of the endotracheal tube projects 4 cm above the carina. the patient has also received a nasogastric tube. the course of the tube is unremarkable the tip of the tube is not visualized on the image. there is no evidence of complications

bibasilar atelectasis. CvT2DistilGPT2 was only able to identify the feeding tube. At least for this study, CXRMate was able to generate a succinct, intelligible report that was factually more correct than other models with respect to the radiologist’s report.

In Table 9, we show a study where CXRMate attained a low CheXbert F1 score. This study includes several findings identified by the radiologist. While each model was able to identify the pacemaker, its leads, and their location, they all struggled to identify the remaining findings. This example contains multiple CheXbert observations that CXRMate (as well as the other models) performed poorly on in Figure 6, including *lung opacity* (CheXbert F1 of 0.491), *pneumonia* (CheXbert F1 of 0.235), *consolidation* (CheXbert F1 of 0.194), and *lung lesion* (or nodule) (CheXbert F1 of 0.077). CXRMate only identified the consolidation and potential pneumonia; however, the location of the consolidation was inconsistent with the radiologists determination (the radiologist determined that the consolidation was in the right lower lung, whereas CXRMate determined that it was in the right middle lobe). M^2 fact_{ENTNLI} and CvT2DistilGPT2 also failed to identify several of the radiologist’s findings. This demonstrates some of the limitations of current CXR report generation models.

In Table 10, we show a study that highlights the issues caused by the labels of Chen *et al.* (2020). As previously highlighted in Tables 1 and 2, the labels of Chen *et al.* (2020) do not include an impression section and as a result have information loss compared to the original findings sections when there are more than 100 tokens. To show the impact of this on a CXR report generator, we selected a study with a longer radiologist report, and compared it to the report generated by CvT2DistilGPT2, which was the best performing model trained on the labels of Chen *et al.* (2020). First, the impression section was not generated, which is a standard section of a radiologist report. Second, CvT2DistilGPT2 struggled with generating reports of longer length, and was unable to capture any of the findings mentioned in the radiologist’s report. Contrary to this, CXRMate, which was trained on both the findings and impression sections with minimal formatting, was able to generate a longer findings section and capture multiple findings that were mentioned in the radiologist’s report. It also generated the impression section.

5. Limitations and Future Directions

Due to the difficulty in finding publicly-available datasets of quality that also retain longitudinal information between studies, our evaluation was limited to MIMIC-CXR and IU X-ray, the latter of which does not contain longitudinal information. We aim to source additional datasets in future studies of high quality, possibly from a private collection. As with others in the literature, we use the JPG and PNG versions of MIMIC-CXR and IU X-ray, respectively, and resize the images to a lower resolution, which deviates from the quality of the images that a radiologist would be interpreting. Using the DICOM versions of these datasets would reduce quantisation error, while using a higher resolution could reduce the risk of removing fine details. We hypothesise that these factors could be beneficial

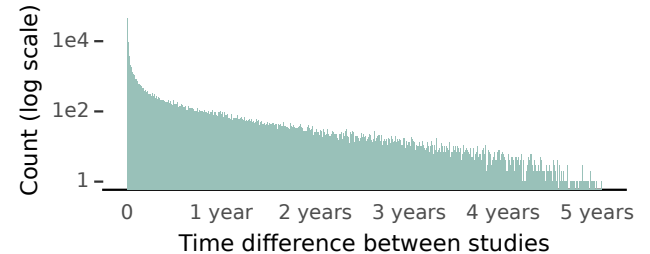


Fig. 8. Histogram of the training split of MIMIC-CXR of time difference between patients’ studies.

for CXR report generation, and should be considered in future work. While our metrics are correlated with radiologists’ assessment of reporting, we aim to source practising radiologists for qualitative evaluation of the generated reports in future investigations. In preliminary testing, we provided the time difference between the current and previous study to the model, however, this had no impact on performance. The time differences between studies from MIMIC-CXR are shown in Figure 8; there can be a large difference in time between studies, which may impact its efficacy as a feature. We also did not consider the images from previous studies, or a history size larger than just the previous study. We aim to explore these in future investigations. The CXR-BERT reward in its current form can lead to repetitions in the generated report for some training runs. We aim to mitigate this by adding a brevity penalty.

6. Conclusion

We demonstrate that our proposed model, CXRMate, generates radiology reports that are more closely aligned with those of radiologists than current state-of-the-art models, such as those leveraging LLMs, reinforcement learning, and multi-task learning. We also demonstrate that conditioning on longitudinal data, and on all images of a study, improves CXR report generation. Moreover, we show that the CXR-BERT reward is a promising alternative to the state-of-the-art RadGraph ER reward. We also demonstrate that differentiating each section with section embeddings improves CXR report generation. Furthermore, we highlight issues pertaining to the evaluation of a large portion of CXR report generators in the literature, caused by excessive formatting. Finally, we open source CXRMate to encourage reproducibility. By improving diagnostic accuracy, we hope that CXRMate brings CXR report generation a step closer to clinical trial consideration.

References

- Bailey, C.R., Bailey, A.M., McKenney, A.S., Weiss, C.R., 2022. Understanding and Appreciating Burnout in Radiologists. *RadioGraphics* 42, E137–E139.
- Boecking, B., Usuyama, N., Bannur, S., Castro, D.C., Schwaighofer, A., Hyland, S., Wetscherek, M., Naumann, T., Nori, A., Alvarez-Valle, J., Poon, H., Oktay, O., 2022. Making the Most of Text Semantics to Improve Biomedical Vision-Language Processing, in: *ECCV*, pp. 1–21.
- Chen, Z., Shen, Y., Song, Y., Wan, X., 2021. Cross-modal Memory Networks for Radiology Report Generation, in: *IJCNLP*, pp. 5904–5914.
- Chen, Z., Song, Y., Chang, T.H., Wan, X., 2020. Generating Radiology Reports via Memory-driven Transformer, in: *EMNLP*, pp. 1439–1449.

Dalla Serra, F., Wang, C., Deligianni, F., Dalton, J., O’Neil, A., 2023. Controllable Chest X-Ray Report Generation from Longitudinal Representations, in: Findings of the Association for Computational Linguistics: EMNLP, Singapore. pp. 4891–4904.

Delbrouck, J.B., Chambon, P., Bluethgen, C., Tsai, E., Almusa, O., Langlotz, C., 2022. Improving the Factual Correctness of Radiology Report Generation with Semantic Rewards, in: EMNLP, pp. 4348–4360.

Demner-Fushman, D., Kohli, M.D., Rosenman, M.B., Shooshan, S.E., Rodriguez, L., Antani, S., Thoma, G.R., McDonald, C.J., 2016. Preparing a collection of radiology examinations for distribution and retrieval. *Journal of the American Medical Informatics Association* 23, 304–310.

Devlin, J., Chang, M.W., Lee, K., Toutanova, K., 2019. BERT: Pre-training of Deep Bidirectional Transformers for Language Understanding, in: NAACL, pp. 4171–4186.

Elgendi, M., Nasir, M.U., Tang, Q., Smith, D., Grenier, J.P., Batte, C., Spieler, B., Leslie, W.D., Menon, C., Fletcher, R.R., Howard, N., Ward, R., Parker, W., Nicolaou, S., 2021. The Effectiveness of Image Augmentation in Deep Learning Networks for Detecting COVID-19: A Geometric Transformation Perspective. *Frontiers in Medicine* 8.

Gaber, K.A., McGavin, C.R., Wells, I.P., 2005. Lateral Chest X-Ray for Physicians. *Journal of the Royal Society of Medicine* 98, 310–312.

Hu, E.J., Shen, Y., Wallis, P., Allen-Zhu, Z., Li, Y., Wang, S., Wang, L., Chen, W., 2022. LoRA: Low-rank adaptation of large language models, in: ICLR.

Irvin, J., Rajpurkar, P., Ko, M., Yu, Y., Ciurea-Ilcus, S., Chute, C., Marklund, H., Haghgoor, B., Ball, R., Shpanskaya, K., Seekins, J., Mong, D.A., Halaibi, S.S., Sandberg, J.K., Jones, R., Larson, D.B., Langlotz, C.P., Patel, B.N., Lungren, M.P., Ng, A.Y., 2019. CheXpert: A Large Chest Radiograph Dataset with Uncertainty Labels and Expert Comparison, in: AAAI, pp. 590–597.

Jain, S., Agrawal, A., Saporta, A., Truong, S., Duong, D.N., Bui, T., Chambon, P., Zhang, Y., Lungren, M.P., Ng, A.Y., Langlotz, C., Rajpurkar, P., 2021. RadGraph: Extracting Clinical Entities and Relations from Radiology Reports, in: NeurIPS Datasets and Benchmarks Track (Round 1).

Johnson, A.E.W., Pollard, T.J., Greenbaum, N.R., Lungren, M.P., Deng, C.y., Peng, Y., Lu, Z., Mark, R.G., Berkowitz, S.J., Horng, S., 2019. MIMIC-CXR-JPG, a large publicly available database of labeled chest radiographs. PhysioNet.

Johnson, A.E.W., Pollard, T.J., Shen, L., Lehman, L.W.H., Feng, M., Ghassemi, M., Moody, B., Szolovits, P., Anthony Celi, L., Mark, R.G., 2016. MIMIC-III, a freely accessible critical care database. *Scientific Data* 3, 160035.

Jones, C.M., Buchlak, Q.D., Oakden-Rayner, L., Milne, M., Seah, J., Esmaili, N., Hachey, B., 2021. Chest radiographs and machine learning – Past, present and future. *Journal of Medical Imaging and Radiation Oncology* 65, 538–544.

Kelly, B., 2012. The chest radiograph. *The Ulster Medical Journal* 81, 143–148.

Lee, H., Lee, D.Y., Kim, W., Kim, J.H., Kim, T., Kim, J., Sunwoo, L., Choi, E., 2023. UniXGen: A Unified Vision-Language Model for Multi-View Chest X-ray Generation and Report Generation. ArXiv:2302.12172 [cs, eess].

Lee, S., Kim, W.J., Chang, J., Ye, J.C., 2024. LLM-CXR: Instruction-Finetuned LLM for CXR Image Understanding and Generation, in: ICLR.

Li, C., Wong, C., Zhang, S., Usuyama, N., Liu, H., Yang, J., Naumann, T., Poon, H., Gao, J., 2023. LLaVA-Med: Training a Large Language-and-Vision Assistant for Biomedicine in One Day, in: NeurIPS Datasets and Benchmarks Track.

Lin, C.Y., Hovy, E., 2003. Automatic evaluation of summaries using N-gram co-occurrence statistics, in: NAACL, pp. 71–78.

Liu, G., Hsu, T.M.H., McDermott, M., Boag, W., Weng, W.H., Szolovits, P., Ghassemi, M., 2019. Clinically accurate chest X-ray report generation, in: MLHC, pp. 249–269.

Loshchilov, I., Hutter, F., 2022. Decoupled Weight Decay Regularization, in: ICLR.

Miura, Y., Zhang, Y., Tsai, E., Langlotz, C., Jurafsky, D., 2021. Improving Factual Completeness and Consistency of Image-to-Text Radiology Report Generation, in: NAACL, pp. 5288–5304.

Moor, M., Huang, Q., Wu, S., Yasunaga, M., Zakka, C., Dalmia, Y., Reis, E.P., Rajpurkar, P., Leskovec, J., 2023. Med-Flamingo: a Multimodal Medical Few-shot Learner. ArXiv:2307.15189 [cs].

Najdenkoska, I., Zhen, X., Worring, M., Shao, L., 2022. Uncertainty-aware report generation for chest X-rays by variational topic inference. *Medical Image Analysis* 82, 102603.

Nicolson, A., Dowling, J., Koopman, B., 2023. Improving chest X-ray report generation by leveraging warm starting. *Artificial Intelligence in Medicine* 144, 102633.

Papineni, K., Roukos, S., Ward, T., Zhu, W.J., 2001. BLEU: a method for automatic evaluation of machine translation, in: ACL, p. 311.

Rennie, S.J., Marcheret, E., Mroueh, Y., Ross, J., Goel, V., 2017. Self-Critical Sequence Training for Image Captioning, in: CVPR, pp. 1179–1195.

Shen, D., 2021. Grand Challenges in Radiology. *Frontiers in Radiology* 1.

Smit, A., Jain, S., Rajpurkar, P., Pareek, A., Ng, A., Lungren, M., 2020. Combining Automatic Labelers and Expert Annotations for Accurate Radiology Report Labeling Using BERT, in: EMNLP, pp. 1500–1519.

Thawkar, O., Shaker, A., Mullappilly, S.S., Cholakkal, H., Anwer, R.M., Khan, S., Laaksonen, J., Khan, F.S., 2023. XrayGPT: Chest Radiographs Summarization using Medical Vision-Language Models. ArXiv:2306.07971 [cs].

Touvron, H., Martin, L., Stone, K., Albert, P., Almahairi, A., Babaei, Y., Bashlykov, N., Batra, S., Bhargava, P., Bhosale, S., Bikel, D., Blecher, L., Ferrer, C.C., Chen, M., Cucurull, G., Esiobu, D., Fernandes, J., Fu, J., Fu, W., Fuller, B., Gao, C., Goswami, V., Goyal, N., Hartshorn, A., Hosseini, S., Hou, R., Inan, H., Kardas, M., Kerkez, V., Khabsa, M., Kloumann, I., Korenrev, A., Koura, P.S., Lachaux, M.A., Lavril, T., Lee, J., Liskovich, D., Lu, Y., Mao, Y., Martinet, X., Mihaylov, T., Mishra, P., Molybog, I., Nie, Y., Poultan, A., Reizenstein, J., Rungta, R., Saladi, K., Schelten, A., Silva, R., Smith, E.M., Subramanian, R., Tan, X.E., Tang, B., Taylor, R., Williams, A., Kuan, J.X., Xu, P., Yan, Z., Zarov, I., Zhang, Y., Fan, A., Kambadur, M., Narang, S., Rodriguez, A., Stojnic, R., Edunov, S., Scialom, T., 2023. Llama 2: Open Foundation and Fine-Tuned Chat Models. ArXiv:2307.09288 [cs].

Vedantam, R., Lawrence Zitnick, C., Parikh, D., 2015. CIDEr: Consensus-Based Image Description Evaluation, in: CVPR, pp. 4566–4575.

Wang, C., Cho, K., Gu, J., 2020. Neural machine translation with byte-level subwords, in: AAAI, pp. 9154–9160.

Williams, R.J., Zipser, D., 1989. A Learning Algorithm for Continually Running Fully Recurrent Neural Networks. *Neural Computation* 1, 270–280.

Wu, H., Xiao, B., Codella, N., Liu, M., Dai, X., Yuan, L., Zhang, L., 2021. CVT: Introducing Convolutions to Vision Transformers, in: ICCV, pp. 22–31.

Wu, X., Yang, S., Qiu, Z., Ge, S., Yan, Y., Wu, X., Zheng, Y., Zhou, S.K., Xiao, L., 2022. DeltaNet: Conditional Medical Report Generation for COVID-19 Diagnosis, in: ICCL, pp. 2952–2961.

Yan, A., He, Z., Lu, X., Du, J., Chang, E., Gentili, A., McAuley, J., Hsu, C.N., 2021. Weakly Supervised Contrastive Learning for Chest X-Ray Report Generation, in: EMNLP, pp. 4009–4015.

Yang, L., Wang, Z., Zhou, L., 2023. MedXChat: Bridging CXR Modalities with a Unified Multimodal Large Model. ArXiv:2312.02233 [cs].

Yu, F., Endo, M., Krishnan, R., Pan, I., Tsai, A., Reis, E.P., Fonseca, E.K.U.N., Lee, H.M.H., Abad, Z.S.H., Ng, A.Y., Langlotz, C.P., Venugopal, V.K., Rajpurkar, P., 2023. Evaluating progress in automatic chest X-ray radiology report generation. *Patterns* , 100802.

Zhang, T., Kishore, V., Wu, F., Weinberger, K.Q., Artzi, Y., 2020. BERTScore: Evaluating Text Generation with BERT, in: ICLR.

Zhu, Q., Mathai, T.S., Mukherjee, P., Peng, Y., Summers, R.M., Lu, Z., 2023. Utilizing Longitudinal Chest X-Rays and Reports to Pre-fill Radiology Reports, in: MICCAI. volume 14224, pp. 189–198.